ACS APPLIED NANO MATERIALS
Cite This: ACS Appl. Nano Mater. 2019, 2, 1940−1950
Article
www.acsanm.org

Exchange Bias in Bulk α-Fe/γ-$Fe_{70}Mn_{30}$ Nanocomposites for Permanent Magnet Applications

I. J. McDonald,*,† M. E. Jamer,‡,§ K. L. Krycka,‡ E. Anber,∥ D. Foley,∥ A. C. Lang,∥ W. D. Ratcliff,‡ D. Heiman,⊥ M. L. Taheri,∥ J. A. Borchers,‡ and L. H. Lewis†

†Department of Chemical Engineering and ⊥Department of Physics, Northeastern University, Boston, Massachusetts 02115, United States

‡NIST Center for Neutron Research, National Institute of Standards and Technology, Gaithersburg, Maryland 20899, United States

§Department of Physics, United States Naval Academy, Annapolis, Maryland 21402, United States

∥Department of Materials Science and Engineering, Drexel University, Philadelphia, Pennsylvania 19104, United States

ABSTRACT: Here we report on the microstructural factors influencing the formation of the interfacial exchange bias effect in three-dimensional transition-metal-based nanocomposite systems, with relevance to permanent magnet applications. Bulk phase-separated nanocomposites consisting of the ferromagnetic α-Fe and metastable antiferromagnetic γ-$Fe_{70}Mn_{30}$ phases exhibit a notable low-temperature exchange bias and substantial coercivity ($\mathbf{H_{ex}}$ = 24.6 kA/m, $\mathbf{H_C}$ = 95.7 kA/m) as well as a near room-temperature blocking temperature. Structural investigation by synchrotron X-ray diffraction, neutron scattering, and transmission electron microscopy confirm that the ferromagnetic α-Fe phase nucleates as small precipitates ($d \approx 50$ nm) at the grain boundaries of the antiferromagnetic γ-$Fe_{70}Mn_{30}$ grains (d = 360−740 nm) and grows anisotropically upon heat treatment, resulting in an elliptical geometry. These results indicate that optimization of the exchange bias effect in bulk nanocomposite systems may be achieved through maximizing the surface-to-volume ratio of ferromagnetic precipitates in an antiferromagnetic matrix, enhancing the magnetocrystalline anisotropy of the antiferromagnetic phase to facilitate interfacial pinning and ensuring a balanced distribution of the ferromagnetic and antiferromagnetic phases. This work further clarifies critical factors influencing the formation of an exchange bias in an inexpensive transition-metal-based bulk nanocomposite system with potential for scalable production.

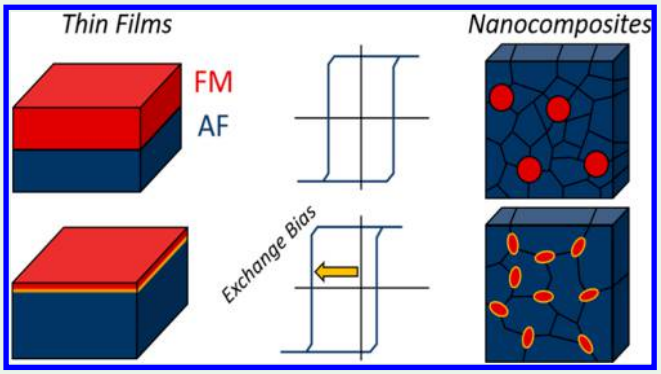

KEYWORDS: *exchange bias, magnetism, magnetic coupling, nanocomposite, microstructure, synchrotron X-ray diffraction, neutron scattering*

1. INTRODUCTION

Unidirectional anisotropy produced by the exchange bias effect has found wide use in several noteworthy thin-film device architectures ranging from magnetic recording media to magnetoresistive devices.[1,2] This unidirectional anisotropy is observed in many diverse magnetic composite systems including ferromagnetic (FM)/antiferromagnetic (AF),[3,4] FM/ferrimagnetic (FI),[5] and hard FM/soft FM systems[6] and is commonly attributed to exchange interactions occurring at the interface between these magnetic phases.[1] For this study, the FM/AF-type of composite system will be the focus. The exchange bias effect results in an asymmetric shift ($\mathbf{H_{ex}}$) of the magnetization $\mathbf{M(H)}$ loop along the field axis after field-cooling from a temperature greater than the AF Néel temperature but lower than the FM Curie temperature.[1] In thin-film exchange-biased systems, it has been shown that the magnitude of the exchange bias is conditional on the relative thicknesses of each thin-film layer; exchange bias is known to be inversely proportional to the FM thickness (reaching a maximum at sub-10 nm film thicknesses).[3,4] The role of the AF thickness on exchange bias is much more complex.[1,3,4] While studied extensively in oxide-coated particles and two-dimensional (2D) bilayer thin-film systems, research into the exchange-bias effect in bulk nanocomposite systems has been limited.[1,2,7−12] Consequently, many key exchange bias parameters that are well-understood for thin-film systems have yet to be fully considered in bulk three-dimensional (3D) exchange-biased systems. Understanding these influencing factors in bulk systems is necessary for the development of present-day applications such as novel permanent magnets based on the exchange bias effect,[1,2,7−9] as first proposed by Meiklejohn and Bean in 1957.[13]

Received: December 27, 2018
Accepted: February 15, 2019
Published: February 15, 2019

DOI: 10.1021/acsanm.8b02319
ACS Appl. Nano Mater. 2019, 2, 1940−1950

Exchange bias studies have been largely confined to thin-film bilayers and oxide core−shell nanoparticles with far fewer reports of exchange bias in 3D bulk intermetallic alloys.[7,9,14−19] Early work by Kouvel et al. examined a number of single-phase, binary alloy systems (Ni−Mn, Fe−Mn, Cu−Mn, Ag−Mn) made by standard solidification methods and attributed the noted exchange bias in these alloys to composition fluctuations or to spin-glass-like states.[14,17] Recent studies on the Heusler family of alloys reported an exchange bias, also attributed to composition fluctuations, that produced coexisting magnetic phases.[15,16] Khan et al. found that the exchange bias and blocking temperature (i.e., the temperature where the exchange bias effect disappears) both scale with Mn content in the $Ni_{50}Mn_{25+x}Sb_{25-x}$ Heusler alloy.[15] Further studies have examined the relationship between microstructure and the exchange bias effect in various oxide systems generated via mechanical mixing,[20−22] reduction reaction,[23] or high-temperature phase precipitation[24,25] to obtain a two-phase microstructure. Dobrynin et al. examined the formation of an exchange anisotropy in Co−CoO core−shell nanoparticles embedded in a noninteracting Al_2O_3 matrix, finding the surface-to-volume ratio of the nanoparticles to be a crucial factor in determining the balance of interfacial exchange energy to volume-proportional Zeeman energy.[26] Anhøj et al. studied the Fe−Mn binary alloy system as well, examining how the ratio of the FM to AF phase in a ball-milled nanocomposite affected the coercivity and exchange bias.[27] This study, however, focused on the ratio of the FM to AF phase and did not address the effect of grain size. More recently, Nayak et al. offered up a new approach to designing Mn−Fe−Ga Heulser alloys with a large theoretical exchange bias that would stabilize the second quadrant magnetization, making it useful as material for rare-earth-free permanent magnets.[28] However, their study concluded that further work is required to find the optimal microstructure to maximize coercivity as well as the total magnetization. Similarly, contemporary studies have examined $CoFe/CoFe_2O_4$ core−shell nanoparticles with specific application in the permanent magnet industry; many of these studies advocate for further research into the optimal microstructure.[29−31]

In this work, $Fe_{70}Mn_{30}$ nanocomposites are synthesized via melt-spinning. The Fe−Mn alloy system was chosen, as it demonstrates the unique ability to form both the AF γ-FeMn phase, well-studied as one of the most widely used AF materials for exchange-biased thin-film architectures,[3,32−35] and the FM α-Fe phase, recognized for its role in the steel industry.[10,36,37] The $Fe_{70}Mn_{30}$ composition is chosen to access the mixed (α-Fe + γ-FeMn) two-phase region of the Fe−Mn binary alloy phase diagram.[38] Melt-spinning is then utilized both to retain these nonequilibrium phases at room temperature and to restrict grain growth, producing a nanoscaled microstructure. The α-Fe phase has a body-centered cubic crystal structure ($Im\bar{3}m$ space group) and unit cell lattice parameter of a = 2.866 Å that exists below T = 1185 K and can accommodate up to ∼3 wt % Mn under equilibrium conditions.[39] The pure α-Fe phase is FM with a room-temperature saturation magnetization $\mathbf{M}_s$ = 217 A·m^2/kg (217 emu/g) and Curie temperature T_C = 1043 K; however, both saturation magnetization and Curie temperature are reduced linearly with dilute additions of Mn.[40] At high temperatures (T ≈ 1400 K), γ-FeMn is the equilibrium phase across all Mn concentrations but is only energetically favorable in a limited range of intermediate Mn content (∼5−70%) for T < 1400 K. Outside of this range, the γ-FeMn phase may be stabilized to room temperature by rapid solidification or by the addition of a ternary alloying element.[41] The γ-FeMn phase is AF with the face-centered cubic structure ($Fm\bar{3}m$ space group). The lattice parameter and Néel temperature of γ-FeMn both increase with increased Mn content.[42−51] Finally, the ε-FeMn phase is a nonequilibrium phase with the hexagonal close packed crystal structure ($P6_3/mmc$ space group) that is reported to form within 10 < x < 30 wt % Mn.[52] The ε-FeMn phase has also been shown to be AF with a Néel temperature of roughly $T_N \approx$ 230 K that is generally independent of composition.[42] In this work, we identify structure−magnetic property relationships in an $Fe_{70}Mn_{30}$ bulk nanocomposite to clarify the microstructural factors contributing to the formation of the exchange bias effect in an inexpensive transition-metal-based bulk nanocomposite with high industrial scalability.

2. EXPERIMENTAL METHODS

This section provides experimental details of the synthesis and characterization of the bulk nanocomposite $Fe_{70}Mn_{30}$. Bulk ingots (m = 5 g) of nominal $Fe_{70}Mn_{30}$ composition were synthesized by arc-melting (Edmund Buhler MAM-1 mini-arc-melting system[53]) in an argon atmosphere from Mn and Fe granules (Alfa Aesar,[53] 99.98%). Excess Mn (∼4−8 wt %) was intentionally added to the stoichiometric amount to compensate for Mn mass loss by vaporization during the melting process. The ingots were remelted three times to aid with homogenization. Rapid solidification was then employed to access the high-temperature γ-FeMn phase and to restrict grain growth to the nanoscale, therefore maximizing the interfacial area. The bulk arc-melted $Fe_{70}Mn_{30}$ ingot was rapidly solidified via melt-spinning (Edmund Buhler GmbH melt-spinner[53]) in an argon environment using an amorphous silica crucible at an 8 mm distance from the water-cooled copper wheel (31 m/s). This synthesis technique is a widely used industrial process for generating bulk amorphous metals. The nominal chemical composition of the melt-spun ribbons was confirmed using energy-dispersive X-ray spectroscopy (EDS). Samples were heat-treated (T_{HT} = 450, 600, and 900 K; hold time was <4 min) and field-cooled to low temperature (T = 2 K) in an applied magnetic field of $\boldsymbol{\mu}_0\mathbf{H}$ = 1 T under vacuum (10^{-6} Torr) using a Quantum Design Vibrating Sample Magnetometer[53] with a high-temperature oven attachment in order to develop the microstructure. These heat-treatment temperatures were chosen based on key temperatures determined through $\mathbf{M}(\mathbf{T})$ measurements (Figure 1) that will be discussed in further detail.

Magnetic characterization of all samples was performed using vibrating sample magnetometry (VSM, Quantum Design VersaLab[53]) and superconducting quantum interference device (SQUID, Quantum Design MPMS[53]) magnetometry in fields of $-3\ \mathrm{T} \le \boldsymbol{\mu}_0\mathbf{H} \le 3\ \mathrm{T}$ and in the temperature range of $2\ \mathrm{K} \le T \le 1000\ \mathrm{K}$. The magnetic field was applied parallel to the long axis of the ribbon samples, requiring no demagnetization correction. Estimates of the room-temperature FM phase fractions (by mass) were calculated using magnetometry data by subtracting the linear high-field susceptibility from magnetic hysteresis measurements, isolating the FM contribution. The room-temperature saturation magnetization of the FM phase was then compared to literature values to determine the phase fraction of the FM phase in each sample.[38,39]

The presence of AF ordering and determination of AF Néel temperatures was achieved through neutron diffraction experiments conducted on the BT-4 Triple-Axis Spectrometer at the NIST Center for Neutron Research (NCNR) at the National Institute of Standards and Technology (NIST); traditional magnetometry is unable to directly confirm antiferromagnetism.[54] Neutron diffraction measurements were performed using a wavelength of λ = 1.6377 Å (30.5 meV) in the temperature range of 100 K < T < 500 K and in zero applied magnetic field. Data were analyzed using OriginLab[53] and Data Analysis and Visualization Environment (DAVE).[55]

DOI: 10.1021/acsanm.8b02319
ACS Appl. Nano Mater. 2019, 2, 1940−1950

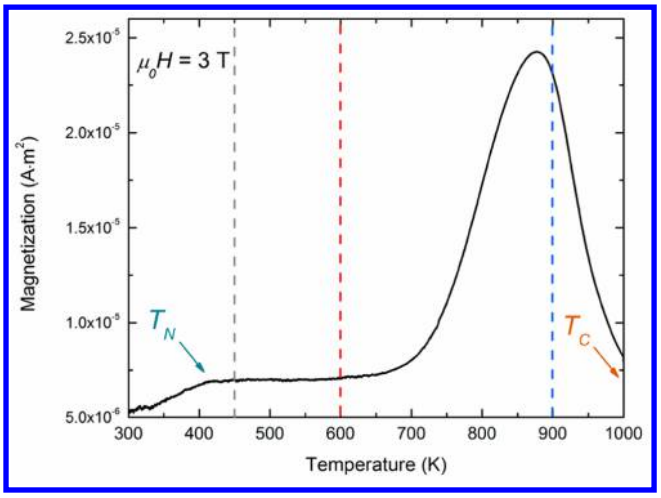

Figure 1. Magnetization as a function of temperature in a saturating field (μ_0**H** = 3 T) for the melt-spun $Fe_{70}Mn_{30}$ as-made sample. The Néel temperature (T_N) and reported Curie temperature (T_C) of the AF and FM phases, respectively, are identified. Dashed lines indicate heat-treatment temperatures.

The structural parameters of the melt-spun ribbons were investigated at room temperature using synchrotron-based X-ray diffraction (XRD), performed at Beamline A2 at the Cornell High Energy Synchrotron Source (CHESS), utilizing high-energy radiation (λ = 0.6277 Å). Measurements were performed using a Diamond <111> Bragg DCM monochromator. The XRD data were indexed and analyzed using a least-squares method,[56] Williamson-Hall analysis,[57] and Rietveld refinement with the crystallography data analysis software program GSAS II[58] to yield lattice parameters, crystallite sizes, phase fractions, and strain values.

The scale and geometry of ferromagnetic precipitates in the $Fe_{70}Mn_{30}$ nanocomposites were determined using small-angle neutron scattering (SANS) experiments performed on the NG7-SANS instrument at the NCNR. All samples were field-cooled prior to measurement at T = 100 K. To assist with isolation of the magnetic scattering, all samples were run in the half-polarization configuration at both magnetic saturation (μ_0**H** = 1.5 T applied parallel to the field-cooling direction and long axis of the ribbons, which corresponds to φ = 0°) and remanence (μ_0**H** = 0 T) conditions. Half-polarization refers to preferentially selecting the neutrons in either the up (↑) or down (↓) polarized state in the incoming beam using a double-V supermirror cavity in combination with an RF neutron spin flipper. In this experiment, three detector settings were used with sample−detector distances of 1, 7, and 15.3 m; the incident beam was not polarized for the 15.3 m setting. The detector was offset horizontally by 25 cm in the 1 m configuration to increase the horizontal q-range. A wavelength of λ = 6 Å was used for the 1 and 7 m configurations, while neutrons with a wavelength of λ = 8 Å and refractive neutron lenses were used in the 15.3 m configuration to reach the lowest possible q-range. The wavelength spread was $\Delta\lambda/\lambda$ = 11.5% for all detector settings. The data were reduced using the NCNR Igor Pro macros[59] containing corrections to account for scattering from the sample cell, background radiation, and variations in the efficiency of detector pixels. The data were then scaled to the intensity of the incident beam, and two-dimensional SANS data were converted to one-dimensional plots of $I(q)$ vs q by averaging over sectors of width ±15°. The sum of the scattering intensity for the two polarization states ((|↑> + |↓>) is dominated by structural contributions, although the projection of the magnetization component perpendicular to the field contributes to sectors at φ = 0°. The projection of the net magnetization parallel to the applied field can be extracted from the difference between the data obtained from the two polarization states (|↓> − |↑>) for sectors at φ = 90°.[60] The reduced sector data were then fit to physical models using the SasView program.[61]

Direct investigation of the bulk nanocomposite microstructure was also conducted using both transmission electron microscopy (TEM) and scanning TEM (STEM). TEM lamella were prepared from annealed samples via an in situ lift-out technique using an FEI DB-235 focused ion beam.[53] A final 5 kV polish was then used to thin samples to electron transparency. Microstructural analysis and phase identification were carried out via TEM and STEM on a JEOL 2100 field-emission TEM.[53] This instrument is also equipped with energy-dispersive X-ray spectroscopy (EDS, Oxford Instruments[53]) for chemical analysis.

3. EXPERIMENTAL RESULTS

3.1. Magnetic Characterization. Details of the magnetic behavior of the bulk nanocomposite were obtained using three characterization techniques: magnetization as a function of temperature, magnetization as a function of applied magnetic field, and neutron diffraction; the results are reported here.

3.1.1. Temperature-Dependent Magnetic Behavior. Critical temperatures of the melt-spun $Fe_{70}Mn_{30}$ samples were identified through measurements of magnetization as a function of temperature, **M(T)**. **M(T)** measurements (recorded at 10 K/min) in a saturating field (μ_0**H** = 3 T), Figure 1, show a very low starting magnetization value that

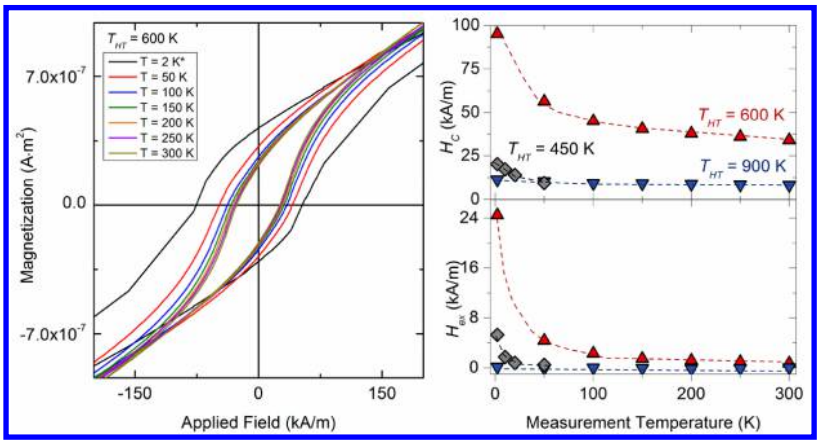

Figure 2. (Left) Magnetic hysteresis measurements of the T_{HT} = 600 K sample taken at various temperatures (2−300 K). *The measurement at T = 2 K was collected with a SQUID magnetometer, all others were taken using VSM. (Right) Observed change in exchange bias ($\mathbf{H}_{ex}$) and coercivity ($\mathbf{H}_C$) of the field-cooled samples as a function of measurement temperature. Error bars are smaller than the symbols; dashed curves act as a guide to the eye.

DOI: 10.1021/acsanm.8b02319
ACS Appl. Nano Mater. 2019, 2, 1940−1950

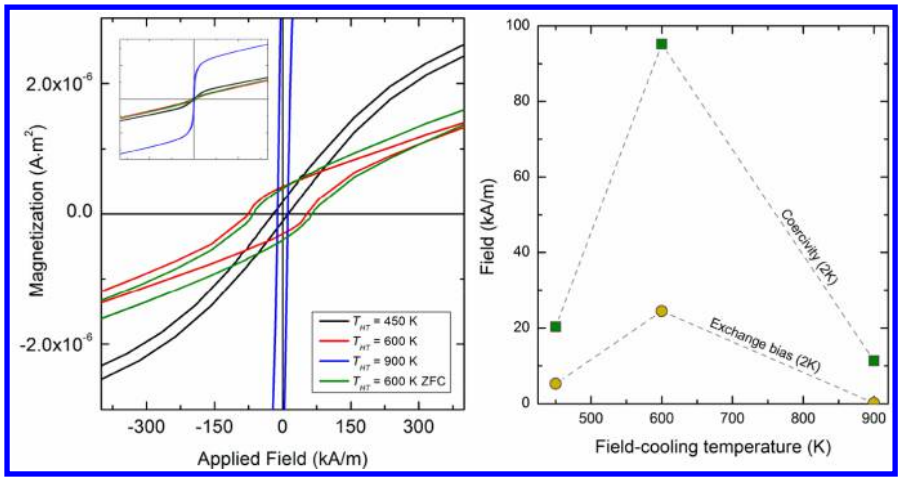

Figure 3. (Left) Magnetic hysteresis measurements taken at T = 2 K of the three field-cooled samples as well as a zero-field-cooled (ZFC) T_{HT} = 600 K sample showing the absence of an exchange bias. Inset: Plot showing a better view of the overall magnetic hysteresis shape for these samples. (Right) Observed change in exchange bias ($\mathbf{H_{ex}}$) and coercivity ($\mathbf{H_C}$) of melt-spun $Fe_{70}Mn_{30}$ ribbons as a function of field-cooling temperature. Dashed lines act as a guide to the eye.

increases gradually to a small feature near T = 425 K, which is associated with the Néel temperature of the high-temperature γ-FeMn phase. Above this temperature, the magnetization remains relatively constant until roughly T = 600 K, when it begins to increase dramatically, suggesting a metastable increase in the phase fraction of the FM α-Fe phase. The magnetization, as a function of the amount of α-Fe present, reaches a maximum at approximately T = 860 K before decreasing rapidly as the temperature approaches the reported Curie temperature of the α-Fe phase (T_C = 1040 K); these critical temperatures are in broad agreement with values reported in literature.[38−40] While the full Curie transition exceeded the temperature capabilities of this instrument, T_C was confirmed through differential scanning calorimetry (not shown). Three heat-treatment temperatures (T_{HT} = 450, 600, 900 K) were chosen based on this $\mathbf{M(T)}$ measurement, corresponding to significant changes in magnetization that are hypothesized to reflect a modification of the microstructure. All heat-treatment temperatures were selected to be greater than the proposed Néel temperature of the AF phase but lower than the proposed Curie temperature of the FM phase in order to fulfill field-cooling requirements.[1]

3.1.2. Field-Dependent Magnetic Behavior. Bulk magnetic properties of field-cooled $Fe_{70}Mn_{30}$ samples including the quantification of the exchange bias effect were provided through volume-averaged magnetization measurements, $\mathbf{M(H)}$. Room-temperature hysteresis curves of all samples consisted of a hysteretic portion (-0.25 T < $\boldsymbol{\mu_0 H}$ < 0.25 T) and linear portions (-0.25 T > $\boldsymbol{\mu_0 H}$ and $\boldsymbol{\mu_0 H}$ > 0.25 T). The hysteretic portion was attributed to the FM α-Fe phase that saturates at an applied field of $\boldsymbol{\mu_0 H}$ = 2 T, and the linear portion was attributed to the AF γ-FeMn phase. In agreement with reports in literature, the magnitudes of the exchange bias effect and the coercivity in these bulk FeMn-based samples are increased with a decrease in temperature following a general $T^{-3/2}$ law,[19,62−64] illustrated in Figure 2; the origin of this effect is the reduction in thermal fluctuations of interfacial spins with lowered temperature.[62,65,66] It is important to note that a nonzero exchange bias was still present at room temperature in the T_{HT} = 600 K sample, indicating a blocking temperature that is near T = 300 K.

An appreciable exchange bias [$\mathbf{H_{ex}}$ = 5.3 kA/m (67 Oe)] and notable coercivity [$\mathbf{H_C}$ = 20.4 kA/m (256 Oe)] were measured at T = 2 K in the sample heat-treated and field-cooled from T_{HT} = 450 K; this effect was absent in zero-field-cooled samples. Heat-treating and field-cooling from an intermediate temperature (T_{HT} = 600 K) resulted in a significant enhancement of both the exchange bias and the coercivity measured at T = 2 K [$\mathbf{H_{ex}}$ = 24.6 kA/m (308 Oe); $\mathbf{H_C}$ = 95.7 kA/m (1200 Oe)]. However, heat-treating at a much higher temperature, T_{HT} = 900 K, resulted in a drastic decrease in exchange bias and coercivity [$\mathbf{H_{ex}}$ = negligible and $\mathbf{H_C}$ = 12.0 kA/m (150 Oe) at T = 2 K]. Figure 3 shows $\mathbf{M(H)}$ measurements for the three field-cooled samples taken at T = 2 K including a zero-field-cooled measurement of the T_{HT} = 600 K sample to illustrate the effect of field-cooling; the evolution of exchange bias and coercivity with increasing heat-treatment temperatures is also summarized in Figure 3.

3.1.3. Characteristics of Antiferromagnetism Derived from Neutron Diffraction. Confirmation of AF ordering in the γ-FeMn phase along with identification of the AF Néel temperature was accomplished through neutron diffraction measurements of heat-treated $Fe_{70}Mn_{30}$ samples. The presence of the AF γ-FeMn phase was verified in all three heat-treated samples by observation of the AF γ-FeMn (110) sublattice peak in zero-field neutron diffraction patterns, present at a position representing half the d-spacing of the structural (220) Bragg peak. A representative neutron diffraction pattern of the T_{HT} = 600 K sample is displayed in Figure 4. The AF (110) sublattice peak was clearly observed at T = 100 K but was fully extinguished at T = 460 K, indicating that the antiferromagnetic alignment has broken down, and the Néel temperature has been exceeded. To accurately determine the Néel temperature of the AF γ-FeMn phase, the intensity of the AF (110) sublattice peak was monitored as a function of temperature (T = 100−460 K) for all heat-treated samples. The change in the AF (110) sublattice peak intensity was then fit to a Brillouin function with the Néel temperature corresponding to the inflection point (Figure 4, inset). The neutron diffraction measurements, along with temperature-dependent magnetic measurements, confirm that the Néel temperature is approximately T_N = 425 ± 9 K for all samples with no significant change due to heat treatment.

DOI: 10.1021/acsanm.8b02319
ACS Appl. Nano Mater. 2019, 2, 1940−1950

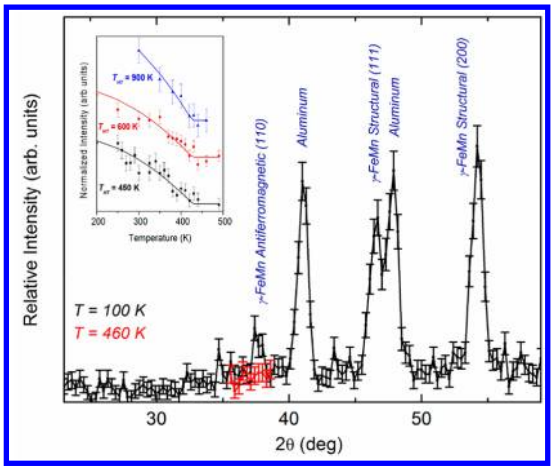

Figure 4. Representative neutron diffraction pattern taken at T = 100 K in zero field for T_{HT} = 600 K showing the structural and antiferromagnetic diffraction peaks of the γ-FeMn phase. A segment of the neutron diffraction pattern for the same sample taken at T = 460 K shows the absence of the AF peak. Inset: Reduction in the intensity of the AF γ-FeMn (110) sublattice peak with temperature near the Néel temperature for all three heat-treated samples. Solid lines show a Brillouin model fit of each data set, and error bars represent one standard deviation.

3.2. Structural Characterization. Identification of relevant structural parameters was performed using three primary characterization techniques: synchrotron X-ray diffraction, neutron scattering, and transmission electron microscopy. No significant structural differences were observed between the as-made ribbons and after heat treatment at T_{HT} = 450 K; thus the as-made and T_{HT} = 450 K samples were considered to be equivalent in this context.

3.2.1. Structural Information Derived from Synchrotron X-ray Diffraction. Structural parameters of the γ-FeMn and α-Fe phases in field-cooled $Fe_{70}Mn_{30}$ samples were identified through synchrotron X-ray diffraction (XRD) measurements. The sample that was heat-treated at T_{HT} = 450 K was confirmed to primarily consist of the high-temperature γ-FeMn phase (Figure 5). The determined lattice parameter of the γ-FeMn phase (a = 3.604 ± 0.001 Å) matched well with expected values for the nominal composition (30 wt % Mn). This sample was found to consist of nanocrystallites with average diameters (<d>) on the order of <d> = 360 ± 40 nm with a small lattice strain (ε = 0.11 ± 0.03%) using Williamson-Hall analysis. With an increased heat-treatment temperature, the lattice parameter and lattice strain of the γ-FeMn phase remained relatively unchanged, but the grain size increased significantly from <d> = 360 ± 40 nm for T_{HT} = 450 K to <d> = 740 ± 160 nm for T_{HT} = 600 K before decreasing to roughly <d> = 570 ± 190 nm for T_{HT} = 900 K. Microstructural information obtained from all heat-treated $Fe_{70}Mn_{30}$ samples is detailed in Table 1.

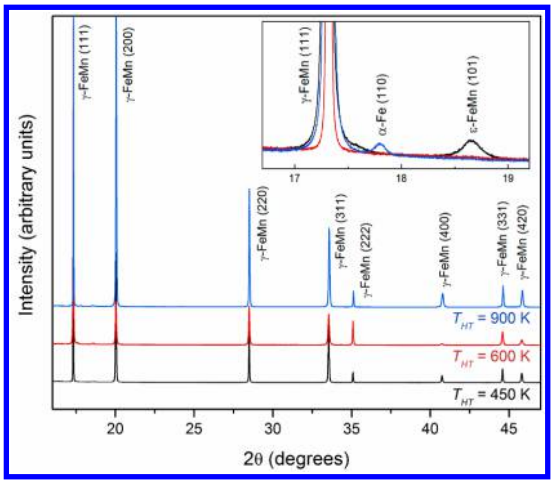

Figure 5. Synchrotron X-ray diffraction (XRD) patterns showing that in the T_{HT} = 450 K and T_{HT} = 600 K samples, only the γ-FeMn and ε-FeMn phases are observed. Inset: Evidence of the α-Fe phase is only resolved after heating to T_{HT} = 900 K. Changes in the broadening of the γ-FeMn (111) Bragg peak are also noted.

Table 1. Microstructural Properties of the Melt-Spun $Fe_{70}Mn_{30}$ Ribbons after Heat Treatment to Various Temperatures[a]

γ-FeMn			
	450 K	600 K	900 K
lattice parameter (Å)	3.604 ± 0.001	3.604 ± 0.001	3.601 ± 0.001
grain size (nm)	360 ± 40	740 ± 160	570 ± 190
strain (%)	0.11 ± 0.03	0.10 ± 0.02	0.10 ± 0.01
α-Fe			
	450 K	600 K	900 K
lattice parameter (Å)	-	-	2.864 ± 0.002
precipitate minor axis (nm)	-	49 ± 14	48 ± 10
precipitate major axis (nm)	-	62 ± 16	171 ± 99
strain (%)	-	-	0.47 ± 0.11
phase fraction (wt %)	0.0100 ± 0.0001	0.0130 ± 0.0001	0.280 ± 0.002
ε-FeMn			
	450 K	600 K	900 K
a lattice parameter (Å)	2.540 ± 0.002	2.542	2.544 ± 0.003
c lattice parameter (Å)	4.096 ± 0.002	4.096 ± 0.002	4.091 ± 0.004
grain size (nm)	70	25	25
strain (%)	0.10 ± 0.10	0.14	0.05 ± 0.03
phase fraction (wt %)	0.019	0.019	0.045

[a]Structural attributes are derived from synchrotron XRD measurements, α-Fe precipitate sizes are obtained from fits of SANS data (for the T_{HT} = 600 and 900 K samples only), and α-Fe phase fraction values are calculated from magnetometry.

The equilibrium α-Fe phase was only apparent in synchrotron XRD measurements following heat treatment at T_{HT} = 900 K (Figure 5, inset). The lattice parameter of the α-Fe phase in the T_{HT} = 900 K sample was determined to be approximately a = 2.864 ± 0.002 Å; this corresponds well with reported values of the α-Fe phase containing no Mn (a = 2.865 Å).[67] In the T_{HT} = 900 K sample, this α-Fe phase was determined to possess an average grain size of <d > = 60 nm along with a significant lattice strain (ε = 0.47 ± 0.11%) using Williamson-Hall analysis and Rietveld refinement; however, this assessment is based on a limited number of diffraction peaks and should be considered speculative. There is also a very small phase fraction (<0.05 wt %) of the nonequilibrium

DOI: 10.1021/acsanm.8b02319
ACS Appl. Nano Mater. 2019, 2, 1940−1950

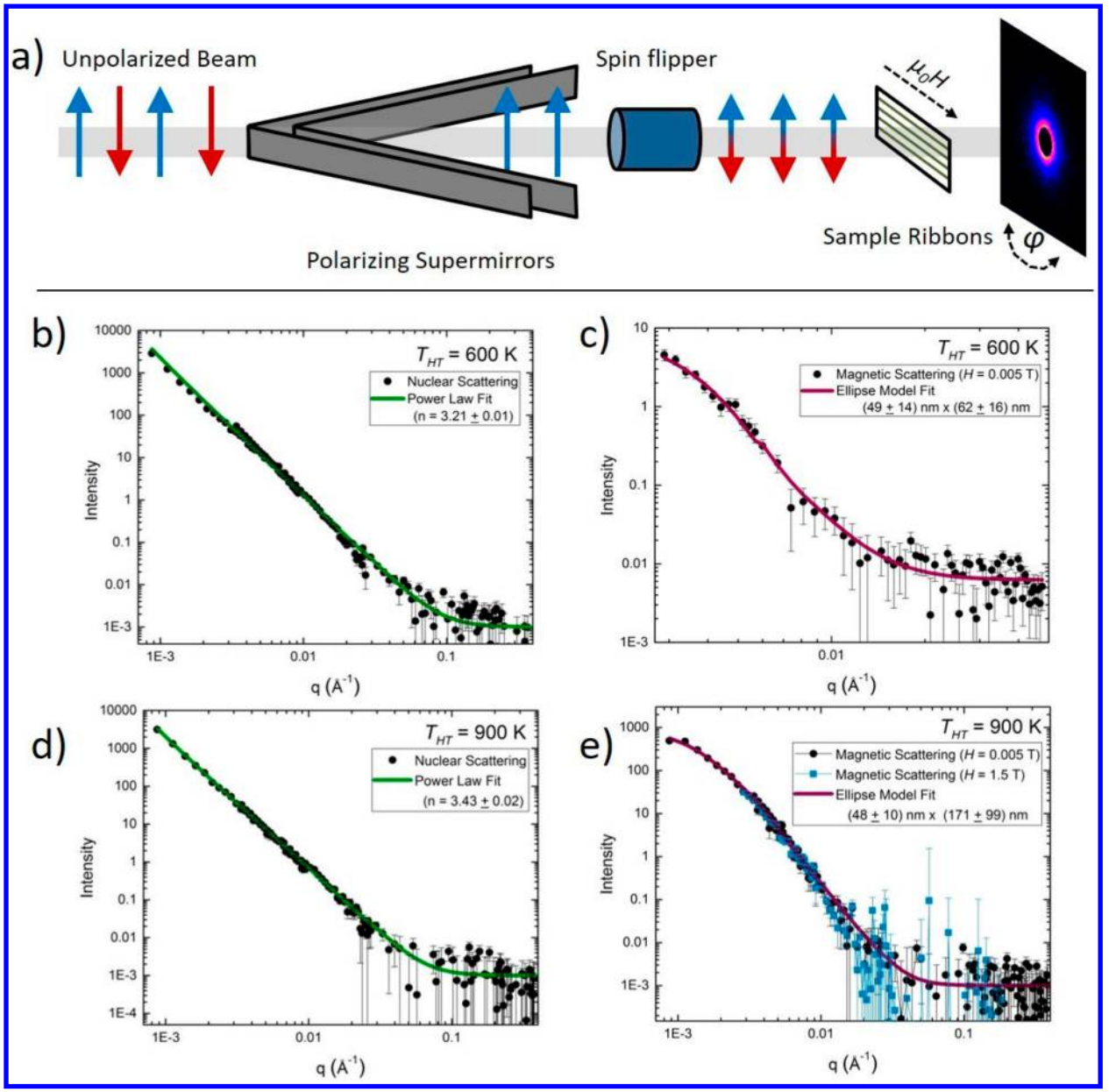

Figure 6. (a) Diagram illustrating the operation of small-angle neutron scattering experiments. Plots of structural scattering intensity versus q fit to a power law show no significant change in Porod slope for both the (b) T_{HT} = 600 K and (d) T_{HT} = 900 K samples. All magnetic scattering for the (c) T_{HT} = 600 K and (e) T_{HT} = 900 K samples was fit to an ellipse model with 33% polydispersity.

hexagonal ε-FeMn phase in all samples. The lattice parameters, grain sizes, and lattice strain of the ε-FeMn phase remain relatively unchanged across all heat-treated samples, as listed in Table 1.

3.2.2. Structural Information Derived from Small-Angle Neutron Scattering. Length scales associated with the ordered FM precipitates in heat-treated $Fe_{70}Mn_{30}$ samples were probed using small-angle neutron scattering (SANS); the instrument scattering geometry is illustrated in Figure 6a. Since neutrons interact with both nuclear and magnetic structure, the resultant scattering provides information about both the grain size and the FM domain size of the α-Fe precipitates. The structural scattering was extracted from the $\varphi = 0°$ sectors for the added polarization states ($|\uparrow\rangle + |\downarrow\rangle$) measured in saturation at T = 100 K, as shown in Figure 6b,d for the T_{HT} = 600 K and T_{HT} = 900 K samples, respectively. Note that the T_{HT} = 450 K sample was omitted due to limitations in SANS measurement sensitivity. The data in both graphs were fit with a power function, $I(Q) = A/Q^n + B$, where A and B are constants, and n is the Porod slope; the Porod slope provides insight into the geometry of the local structure, which is dominated by the γ-FeMn grains in this q-range. The Porod slope was determined to be n = 3.2 and n = 3.4 for T_{HT} = 600 K and T_{HT} = 900 K, respectively. These values suggest that the α-Fe grains have a 3D character with rough interfaces or surfaces, possessing a fractal dimension of approximately 2.7. The similarity of the fits for samples T_{HT} = 600 K and T_{HT} = 900 K suggests that the geometry of the FM α-Fe structures does not change significantly between these two samples.

Information regarding the size and shape of the α-Fe precipitates can be indirectly determined from SANS measurements of the FM domain size in low field under the

DOI: 10.1021/acsanm.8b02319
ACS Appl. Nano Mater. 2019, 2, 1940−1950

assumption that each grain consists of a single magnetic domain. Magnetic scattering from the FM precipitates in the T_{HT} = 600 K sample was isolated by subtracting the sum of the |↑> and |↓> polarization state data obtained in the saturated state (which is purely of structural origin) from the sum of |↑> and |↓> data obtained at remanence. To determine length scales associated with the magnetic domains present at low field, the resulting data for the T_{HT} = 600 K samples were fit to a model representing the precipitates as ellipsoids. The magnetic scattering from the α-Fe precipitates in the T_{HT} = 600 K sample was very weak, necessitating circular averaging, rather than the typical sector averaging. These data (Figure 6c) were consistent with an ellipsoid model of the precipitates with radii of 49 ± 14 and 62 ± 16 nm and a corresponding polydispersity (i.e., half-width/average radius) of 33%. It is notable that at high q, the T_{HT} = 600 K scattering is nonzero, flat, and higher than that measured for the sample heat-treated at T_{HT} = 900 K. It is thus possible that this high-q scattering originated from magnetic features with a length scale that is smaller than that detectable by this SANS measurement (<4 nm), suggesting some level of inhomogeneity.

The low-field magnetic scattering from the FM inclusions in the T_{HT} = 900 K sample was also isolated by subtracting the sum of data obtained from the |↑> and |↓> states in saturation from the sum measured at remanence at φ = 0°, as shown in Figure 6e.[68] The average ellipse radii obtained from the fit are 48 ± 10 and 171 ± 99 nm with a corresponding polydispersity of 33%. The smaller domain length scale is roughly consistent with the average structural grain size of $\langle d \rangle \approx$ 60 nm determined from synchrotron X-ray diffraction data for this sample, and the longer length scale suggests that the α-Fe precipitates are elongated in one direction (though the fit is not particularly sensitive to the major axis of the ellipse). Using methods described elsewhere,[60] we extracted the square of the net magnetization component parallel to a 1.5 T field from the difference between the |↓> and |↑> cross sections. The magnitude and shape of this scattering match those of the low-field magnetic scattering, shown in Figure 6e, though the polarized data do not extend to the lowest q.

3.2.3. Structural Information Derived from Transmission Electron Microscopy. A more direct and local measurement of the α-Fe phase geometry and location in the $Fe_{70}Mn_{30}$ sample heat-treated at T_{HT} = 900 K was obtained via transmission electron microscopy (TEM) and scanning transmission electron microscopy (STEM). Positive phase identification of the α-Fe precipitates and the γ-FeMn matrix was also achieved using selected area electron diffraction; data are illustrated in Figure 7. Local regions containing small precipitates ($\langle d \rangle$ = 34 ± 4 nm) of α-Fe with a rough outer surface were observed at the triple points and grain boundaries of the larger γ-FeMn grains (Figure 7, inset). The geometry of the α-Fe precipitates observed with TEM is smaller than that indicated by synchrotron XRD and SANS measurements; this discrepancy is attributed to the highly localized nature of the TEM probe imaging a two-dimensional cross section and inhomogeneity in the samples. Energy-dispersive electron spectroscopy (EDS) also confirmed the nominal composition of the γ-FeMn phase to be approximately 30 ± 3 wt % Mn.

4. DISCUSSION

These data, collected from a wide variety of both direct and indirect characterization methods, confirm attainment of a two-phase nanocomposite of majority phase AF γ-$Fe_{70}Mn_{30}$

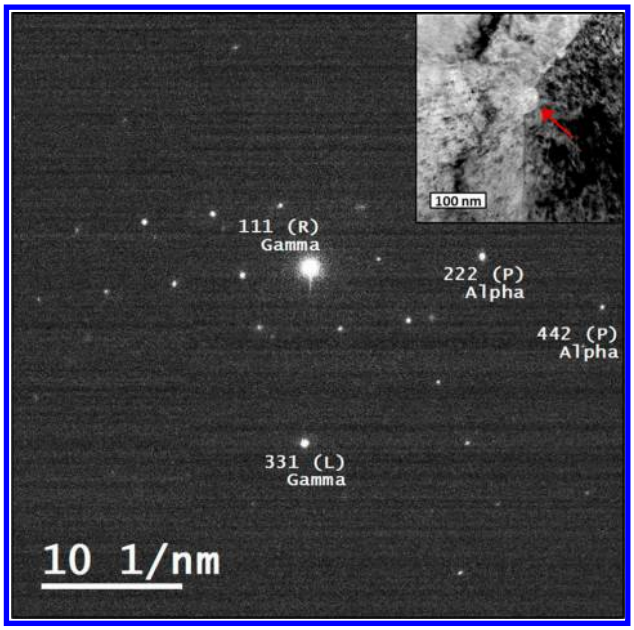

Figure 7. Selected area electron diffraction performed on an α-Fe precipitate located at the grain boundary of the γ-$Fe_{70}Mn_{30}$ matrix. Inset: Transmission electron microscopy image of the γ-FeMn grain boundary showing the (arrow) intergranular precipitation of α-Fe. Reflections for the (R) right-hand and (L) left-hand γ-$Fe_{70}Mn_{30}$ grains as well as the (P) α-Fe precipitate are indexed to identify these phases.

with a small volume of FM α-Fe that precipitates and grows along the grain boundaries of the majority phase. The observed exchange bias in the bulk nanocomposite $Fe_{70}Mn_{30}$ is attributed to the coexistence of the FM α-Fe and the AF γ-$Fe_{70}Mn_{30}$ phases. While the authors acknowledge that an exchange bias may be formed through the interaction of many diverse and varied magnetic phases, the experimental evidence presented here points to the most likely origin of the exchange bias being the interaction between these two primary phases. The lattice parameter of the AF majority γ-FeMn phase (a = 3.604 ± 0.001 Å) undergoes no significant change with heat treatment, indicating a constant composition across all heat-treated samples. In accordance with reported data from the literature, this phase has an approximate composition of γ-$Fe_{74\pm1.7}Mn_{26\pm1.7}$.[42−51] The Néel temperature of the AF γ-FeMn phase (T_N = 425 ± 9 K) also remains constant with heat treatment and, in accordance with literature values, matches the T_N expected for an approximate composition of γ-$Fe_{70\pm1.6}Mn_{30\pm1.6}$.[42−51] These two calculated compositions are consistent with nominal values for the starting composition as well as with the overall composition determined by STEM−EDS. Furthermore, the calculated lattice parameter of the minority FM α-Fe phase present in all heat-treated $Fe_{70}Mn_{30}$ samples indicates no substantial Mn content within the α-Fe phase. Under the assumption that this nominally pure α-Fe phase was the sole FM phase present in all samples, the α-Fe phase fraction f_{FM} was computed as f_{FM} = 0.01 ± 0.0001 wt % for T_{HT} = 450 K, f_{FM} = 0.013 ± 0.0001 wt % for T_{HT} = 600 K, and f_{FM} = 0.28 ± 0.002 wt % for T_{HT} = 900 K (Table 1). These findings confirm the composition of the bulk α-Fe/γ-$Fe_{70}Mn_{30}$ nanocomposite.

Considering the experimental observations detailed above, a phenomenological model was constructed to describe the microstructure of the bulk nanocomposite $Fe_{70}Mn_{30}$. The

DOI: 10.1021/acsanm.8b02319
ACS Appl. Nano Mater. 2019, 2, 1940−1950

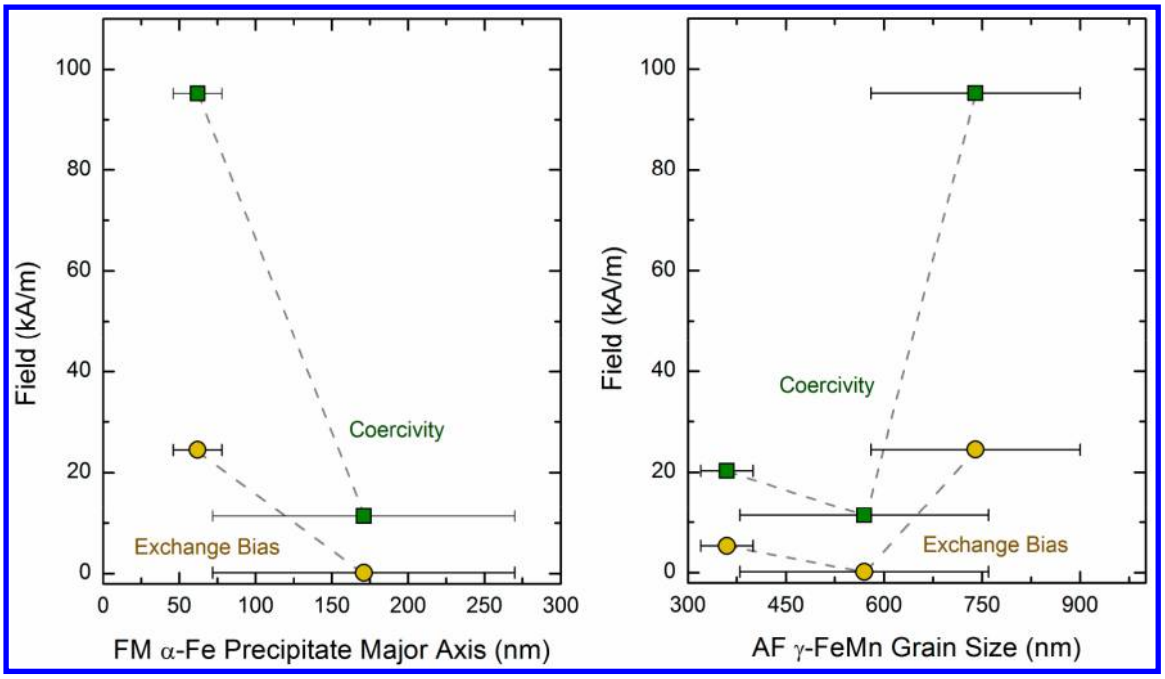

Figure 8. (Left) Change in exchange bias and coercivity (measured at T = 2 K) as a function of the major axis of ellipsoid FM precipitates in the bulk α-Fe/γ-$Fe_{70}Mn_{30}$ nanocomposite as measured by SANS for the T_{HT} = 600 and 900 K samples; this relationship is suggestive of the correlation between FM layer thickness and exchange bias established in thin-film exchange bias literature.[1,75−79] (Right) Change in exchange bias and coercivity (measured at T = 2 K) as a function of AF grain size in bulk α-Fe/γ-$Fe_{70}Mn_{30}$ nanocomposites suggestive of a minimum required grain size for an enhanced exchange bias and coercivity. Despite similarities to comparable thin-film studies, the AF grain size in this bulk system that supports an appreciable exchange bias is significantly larger than the critical AF thickness in FeMn thin-film systems.[32,33] Dashed curves act as a guide to the eye.

minority α-Fe phase is hypothesized to nucleate at the γ-FeMn grain boundaries during rapid solidification.[69,70] These precipitates grow at elevated temperatures, postsolidification, along a preferred direction to produce grains with an elongated elliptical geometry. This intergranular growth produces a generally homogeneous phase distribution, maximizing the total interphase interfacial area and enhancing the exchange bias effect. The even distribution of the FM α-Fe precipitates is also hypothesized to influence both the exchange bias and coercivity. If the precipitates aggregate closely together, they may act as one discrete particle, decreasing the overall interfacial area. However, if they are distributed evenly and throughout the AF matrix, then the interfacial area is maximized and contributes more to the exchange bias. Similarly, the coercivity of an isolated FM particle will increase with a decrease in size toward single domain behavior.[71] If these FM α-Fe precipitates aggregate together, they may begin to interact and behave as one large FM particle, breaking up into many small domains and lowering the coercivity. While FM precipitates in the T_{HT} = 450 K sample are too small to reliably resolve a measure of their dimensions, the minor dimension of the ellipse-shaped grains in the T_{HT} = 600 and 900 K samples remains generally constant (near ∼50 nm) with heat treatment. However, there is a significant increase in the major axis dimension from $\langle d \rangle$ = 62 ± 16 nm after heat treatment at T_{HT} = 600 K to $\langle d \rangle$ = 171 ± 99 nm after heat treatment at T_{HT} = 900 K.

The relative scale of both the FM and AF phases (Table 1) has a direct influence on the development of the total interfacial area, which in turn will determine the magnitude of the exchange bias effect. Further analysis of these above-described trends provides additional insight into how microstructural attributes influence exchange bias in bulk systems as compared to thin-film systems. Studies show that defects at the FM/AF interface influence the exchange bias effect by generating uncompensated spins in the AF material.[19,72−74] The rough surface of the FM precipitates in the present study may lead to an increased density of defects at the FM/AF interface, increasing the magnitude of the exchange bias. For the present bulk nanocomposite samples, the magnitude of the exchange bias effect appears to vary inversely with the major axis dimension of the elliptical FM α-Fe precipitates; the magnitude of the exchange bias is larger at small precipitate sizes ($\langle d \rangle \approx$ 50−60 nm) and seems to be suppressed by excessive growth of the FM phase ($\langle d \rangle \approx$ 170 nm). The apparent decrease in exchange bias at larger FM precipitate sizes is in general agreement with reports of exchange bias in thin-film literature (Figure 8, left).[1,75−79] Here, a decrease in the surface-to-volume ratio with larger FM precipitates seems to lead to a reduction in the overall exchange bias and reflects an imbalance between the exchange energy at the interfaces and the Zeeman energy acting on the FM precipitates.[26]

In this nanocomposite system, a significant exchange bias is observed when the AF grain size is large ($\langle d \rangle$ = 570−740 nm). While this behavior is consistent with the observance of a critical minimum AF thickness reported in select thin-film studies, the scale of the onset AF grain size that supports a significant exchange bias in the present bulk nanocomposite system is approximately 2 orders of magnitude larger than in comparable thin films (Figure 8, right).[4,14,80] We are unable, however, to extract systematically a minimum (or "critical") AF grain size, since the changes observed upon annealing are accompanied by a simultaneous modification of FM precipitate size. It is well-established that the magnetocrystalline

DOI: 10.1021/acsanm.8b02319
ACS Appl. Nano Mater. 2019, 2, 1940−1950

anisotropy of the AF phase plays a major role in the development of an exchange bias.[1,19,81] Here we hypothesize that with no change in the composition of the AF γ-$Fe_{70}Mn_{30}$ phase, any variation in magnetocrystalline anisotropy is a result of microstructural changes. As is concluded by Anhoj et al., an AF phase that is too small may not possess the necessary magnetocrystalline anisotropy to pin the interfacial FM spins and produce an exchange bias.[19,27] In our present system, the AF phase in the T_{HT} = 450 K sample is presumably small in scale with a magnetocrystalline anisotropy value that may be ineffective at pinning the interfacial FM spins. The FM phase in the T_{HT} = 900 K sample is too large in scale, and the small surface-to-volume ratio limits the observable exchange bias effect. The T_{HT} = 600 K sample seems to strike a balance between small FM precipitates with a high surface-to-volume ratio and large AF grains with an adequately high magnetocrystalline anisotropy to produce an observable exchange bias and near room-temperature blocking temperature.

In order to inform future studies on the development of exchange bias in nanocomposite systems, a simple metric for the formation of an exchange bias is proposed. The ratio of the AF grain size (S) to the major axis of the FM precipitate (A) is hypothesized to be an adequate indicator to the observance of an exchange bias. A large S/A ratio signifies either a large AF grain size, a small FM precipitate size, or a combination of both. In the T_{HT} = 900 K sample, S/A = 3.3 ± 2.2, while the T_{HT} = 600 K sample has a much higher S/A value of 11.9 ± 4.0. The T_{HT} = 450 K sample must therefore possess an S/A value that is relatively close to but lower than that of the T_{HT} = 600 K sample; under these assumptions, the major axis of the FM α-Fe precipitates is approximated to be ~30 nm.

5. CONCLUSIONS

In this work, successful synthesis of the α-Fe/γ-$Fe_{70}Mn_{30}$ nanocomposite exhibiting a notable exchange bias allows for the correlation of extrinsic microstructural factors to the development of exchange bias in bulk 3D systems. In this nanocomposite, the FM α-Fe phase forms as small precipitates at the grain boundaries of the AF γ-FeMn phase, thus maximizing the interphase interfacial contact area. In agreement with thin-film literature, the magnitude of the exchange bias effect is suppressed at larger FM volumes. As is the case for some thin-film exchange-biased systems, a minimum AF grain size may be necessary to observe the exchange bias effect. However, the scale of the AF phase in the present bulk samples is approximately 2 orders of magnitude larger than in comparable thin-film systems. The results of this study suggest that optimization of the exchange bias effect in bulk nanocomposite systems may be achieved by limiting growth of FM precipitates (maximizing the surface-to-volume ratio), ensuring sufficiently large AF grains (increasing the magnetocrystalline anisotropy), and producing an adequate distribution of phases. The ratio of the AF grain size to the major axis of the FM precipitate is also introduced as an indicator for the formation of an exchange bias. Continued work should focus on decreasing the growth and ensuring an even distribution of the α-Fe phase through the addition of grain refiners or adjustment of melt-spinning parameters. Furthermore, enhancing the magnetocrystalline anisotropy energy of the AF phase through heat treatment or the addition of a ternary element may result in a lowered minimum AF grain size and an increase in the blocking temperature above room temperature, both factors producing a positive enhancement in exchange bias. Overall, these results point to crucial considerations for the future development of the exchange bias effect in bulk nanocomposite transition-metal alloys.

AUTHOR INFORMATION

Corresponding Author

*E-mail: ian.mcdonald.88@gmail.com.

ORCID

I. J. McDonald: 0000-0002-1261-4013

K. L. Krycka: 0000-0002-6393-3268

Notes

The authors declare no competing financial interest.

ACKNOWLEDGMENTS

This work was primarily supported by the Office of Naval Research grant #N00014-10-1-0553, with some support from the National Science Foundation award ECCS-1402738. We thank S. Disseler for his help with taking measurements on the BT-4 spectrometer at the NCNR. Access to the spin polarization capabilities on the NG7 SANS instrument was provided by the Center for High Resolution Neutron Scattering, a partnership between the National Institute of Standards and Technology and the National Science Foundation under Agreement No. DMR-1508249. This work is based upon research conducted at the Cornell High Energy Synchrotron Source (CHESS) that is supported by the National Science Foundation under award DMR-1332208. We thank Jacob Ruff with his help with taking measurements at CHESS. This work benefited from the use of the SasView application, originally developed under NSF award DMR-0520547. SasView contains code developed with funding from the European Union's Horizon 2020 research and innovation programme under the SINE2020 project, grant agreement No 654000. The authors acknowledge financial support from NSF MRI award # 1429661, and the ARPA-E PNDIODES program.

REFERENCES

(1) Nogues, J.; Schuller, I. K. Exchange Bias. *J. Magn. Magn. Mater.* **1999**, *192*, 203−232.

(2) Jimenez-Villacorta, F.; Lewis, L. H. Advanced Permanent Magnetic Materials. In *Nanomagnetism*; Gonzalez Estevez, J. M., Ed.; One Central Press, 2014; pp 160−189.

(3) Shi, Z.; Du, J; Zhou, S.-M. Exchange Bias in Ferromagnet/Antiferromagnet Bilayers. *Chin. Phys. B* **2014**, *23* (2), 027503.

(4) Jungblut, R.; Coehoorn, R.; Johnson, M. T.; aan de Stegge, J.; Reinders, A. Orientational Dependence of the Exchange Biasing in Molecular-Beam-Epitaxy-Grown $Ni_{80}Fe_{20}/Fe_{50}Mn_{50}$ Bilayers (Invited). *J. Appl. Phys.* **1994**, *75* (10), 6659.

(5) Cain, W. C.; Kryder, M. H. Investigation of the Exchange Mechanism in NiFe-TbCo Bilayers. *J. Appl. Phys.* **1990**, *67* (9), 5722.

(6) Binek, C.; Polisetty, S.; He, X.; Berger, A. Exchange Bias Training Effect in Coupled All Ferromagnetic Bilayer Structures. *Phys. Rev. Lett.* **2006**, *96*, 067201.

(7) Jiménez-Villacorta, F.; Marion, J. L.; Sepehrifar, T.; Daniil, M.; Willard, M. A.; Lewis, L. H. Exchange Anisotropy in the Nanostructured MnAl System. *Appl. Phys. Lett.* **2012**, *100* (11), 112408.

(8) Jiménez-Villacorta, F.; McDonald, I.; Heiman, D.; Lewis, L. H. Tailoring Exchange Coupling and Phase Separation in Fe-Co-Mn Nanocomposites. *J. Appl. Phys.* **2014**, *115* (17), 17A729.

(9) Giri, S.; Patra, M.; Majumdar, S. Exchange Bias Effect in Alloys and Compounds. *J. Phys.: Condens. Matter* **2011**, *23* (7), 073201.

(10) Berkowitz, A. E.; Takano, K. Exchange Anisotropy — a Review. *J. Magn. Magn. Mater.* **1999**, *200* (1−3), 552−570.

DOI: 10.1021/acsanm.8b02319
ACS Appl. Nano Mater. 2019, 2, 1940−1950

(11) Sankaranarayanan, V. K.; Yoon, S. M.; Kim, D. Y.; Kim, C. O.; Kim, C. G. Exchange Bias in NiFe/FeMn/NiFe Trilayers. *J. Appl. Phys.* **2004**, *96* (12), 7428.
(12) Kung, K. T. Y.; Louie, L. K.; Gorman, G. L. MnFe Structure-Exchange Anisotropy Relation in the NiFe/MnFe/NiFe System. *J. Appl. Phys.* **1991**, *69* (8), 5634.
(13) Meiklejohn, W. H.; Bean, C. P. New Magnetic Anisotropy. *Phys. Rev.* **1957**, *105* (3), 904−913.
(14) Kouvel, J. S. A Ferromagnetic-Antiferromagnetic Model for Copper-Manganese and Related Model. *J. Phys. Chem. Solids* **1963**, *24*, 795−822.
(15) Khan, M.; Dubenko, I.; Stadler, S.; Ali, N. Magnetostructural Phase Transitions in $Ni_{50}Mn_{25}+xSb_{25}$-x Heusler Alloys. *J. Phys.: Condens. Matter* **2008**, *20* (23), 235204.
(16) Pathak, A. K.; Khan, M.; Gautam, B. R.; Stadler, S.; Dubenko, I.; Ali, N. Exchange Bias in Bulk Ni−Mn−In-Based Heusler Alloys. *J. Magn. Magn. Mater.* **2009**, *321* (8), 963−965.
(17) Kouvel, J. S. Exchange Anisotropy in Alloys of Composition (Ni, Fe)3Mn. *J. Phys. Chem. Solids* **1960**, *16*, 152−157.
(18) March, N. H.; Lambin, P.; Herman, F. Cooperative Magnetic Properties in Single- and Two-Phase 3d Metallic Alloys Relevant to Exchange and Magnetocrystalline Anisotropy. *J. Magn. Magn. Mater.* **1984**, *44* (1-2), 1−19.
(19) Nogués, J.; Sort, J.; Langlais, V.; Skumryev, V.; Suriñach, S.; Muñoz, J. S.; Baró. Exchange Bias in Nanostructures. *Phys. Rep.* **2005**, *422* (3), 65−117.
(20) Sort, J.; Nogués, J.; Amils, X.; Suriñach, S.; Muñoz, J. S.; Baró, M. D. Room-Temperature Coercivity Enhancement in Mechanically Alloyed Antiferromagnetic-Ferromagnetic Powders. *Appl. Phys. Lett.* **1999**, *75* (20), 3177−3179.
(21) Sort, J.; Nogués, J.; Amils, X.; Suriñach, S.; Muñoz Domínguez, J. S.; Baró, M. D. Correlation between the Microstructure and Enhanced Room Temperature Coercivity in Ball Milled Ferromagnetic - Antiferromagnetic Composites. *Mater. Sci. Forum* **2000**, *343*−*346*, 812−818.
(22) Sort, J.; Nogués, J.; Amils, X.; Suriñach, S.; Muñoz, J. S.; Baró, M. Room Temperature Magnetic Hardening in Mechanically Milled Ferromagnetic−Antiferromagnetic Composites. *J. Magn. Magn. Mater.* **2000**, *219* (1), 53−57.
(23) Sort, J.; Langlais, V.; Doppiu, S.; Dieny, B.; Suriñach, S.; Muñoz, J. S.; Baró, M. D.; Laurent, C.; Nogués, J. Exchange Bias Effects in Fe Nanoparticles Embedded in an Antiferromagnetic Cr2O3Matrix. *Nanotechnology* **2004**, *15* (4), S211−S214.
(24) Tian, Z. M.; Yuan, S. L.; Yin, S. Y.; Liu, L.; He, J. H.; Duan, H. N.; Li, P.; Wang, C. H. Exchange Bias Effect in a Granular System of $NiFe_2O_4$ Nanoparticles Embedded in an Antiferromagnetic NiO Matrix. *Appl. Phys. Lett.* **2008**, *93* (22), 222505.
(25) Chakrabarti, K.; Sarkar, B.; Dev Ashok, V.; Das, K.; Sinha Chaudhuri, S.; Mitra, A.; De, S. K. Exchange Bias Effect in BiFeO3 -NiO Nanocomposite. *J. Appl. Phys.* **2014**, *115* (1), 013906.
(26) Dobrynin, A. N.; Ievlev, D. N.; Temst, K.; Lievens, P.; Margueritat, J.; Gonzalo, J.; Afonso, C. N.; Zhou, S. Q.; Vantomme, A.; Piscopiello, E.; Van Tendeloo, G. Critical Size for Exchange Bias in Ferromagnetic-Antiferromagnetic Particles. *Appl. Phys. Lett.* **2005**, *87* (1), 012501.
(27) Anhøj, T. A.; Jacobsen, C. S.; Mørup, S. Magnetic Properties of $Fe_{1-x}Mn_x$/Fe Nanocomposites. *J. Appl. Phys.* **2004**, *95* (7), 3649−3654.
(28) Nayak, A. K.; Nicklas, M.; Chadov, S.; Khuntia, P.; Shekhar, C.; Kalache, A.; Baenitz, M.; Skourski, Y.; Guduru, V. K.; Puri, A.; Zeitler, U.; Coey, J. M. D.; Felser, C. Design of Compensated Ferrimagnetic Heusler Alloys for Giant Tunable Exchange Bias. *Nat. Mater.* **2015**, *14* (7), 679−684.
(29) Granados-Miralles, C.; Saura-Múzquiz, M.; Andersen, H. L.; Quesada, A.; Ahlburg, J. V.; Dippel, A.-C.; Canévet, E.; Christensen, M. Approaching Ferrite-Based Exchange-Coupled Nanocomposites as Permanent Magnets. *ACS Appl. Nano Mater.* **2018**, *1* (7), 3693−3704.
(30) Lottini, E.; López-Ortega, A.; Bertoni, G.; Turner, S.; Meledina, M.; Van Tendeloo, G.; de Julián Fernández, C.; Sangregorio, C. Strongly Exchange Coupled CorelShell Nanoparticles with High Magnetic Anisotropy: A Strategy toward Rare-Earth-Free Permanent Magnets. *Chem. Mater.* **2016**, *28* (12), 4214−4222.
(31) Quesada, A.; Granados-Miralles, C.; López-Ortega, A.; Erokhin, S.; Lottini, E.; Pedrosa, J.; Bollero, A.; Aragón, A. M.; Rubio-Marcos, F.; Stingaciu, M.; Bertoni, G.; Fernández, C. J.; Sangregorio, C.; de Julián Fernández, C.; Berkov, D.; Christensen, M. Energy Product Enhancement in Imperfectly Exchange-Coupled Nanocomposite Magnets. *Adv. Electron. Mater.* **2016**, *2* (4), 1500365.
(32) Antel, W. J.; Perjeru, F.; Harp, G. R. Spin Structure at the Interface of Exchange Biased FeMn-Co Bilayers. *Phys. Rev. Lett.* **1999**, *83* (7), 1439−1442.
(33) Garcia, F.; Casali, G.; Auffret, S.; Rodmacq, B.; Dieny, B. Exchange Bias in $(Pt/Co_{0.9}Fe_{0.1})_n$/FeMn Multilayers with Perpendicular Magnetic Anisotropy. *J. Appl. Phys.* **2002**, *91* (10), 6905.
(34) Hempstead, R.; Krongelb, S.; Thompson, D. Unidirectional Anisotropy in Nickel-Iron Films by Exchange Coupling with Antiferromagnetic Films. *IEEE Trans. Magn.* **1978**, *14* (5), 521−523.
(35) Gao, T. R.; Shi, Z.; Zhou, S. M.; Chantrell, R.; Asselin, P.; Bai, X. J.; Du, J.; Zhang, Z. Z. Exchange Bias, Training Effect, Hysteretic Behavior of Angular Dependence, and Rotational Hysteresis Loss in NiFe/FeMn Bilayer: Effect of Antiferromagnet Layer Thickness. *J. Appl. Phys.* **2009**, *105* (5), 053913.
(36) Ekholm, M.; Abrikosov, I. A. Structural and Magnetic Ground-State Properties of γ-FeMn Alloys from Ab Initio Calculations. *Phys. Rev. B: Condens. Matter Mater. Phys.* **2011**, *84* (10), 104423.
(37) Allegranza, O.; Chen, M.-M. Effect of Substrate and Antiferromagnetic Film's Thickness on Exchange-Bias Field (Invited). *J. Appl. Phys.* **1993**, *73* (10), 6218.
(38) Predel, B. Fe-Mn (Iron-Manganese) Phase Diagram. *Dy-Er − Fr-Mo* **1995**, *e*, 1−8.
(39) Troiano, A. R.; McGuire, F. T. A Study of the Fe-Rich Fe-Mn Alloys. *Trans. ASM* **1943**, *31* (2), 340−364.
(40) Yamauchi, H.; Watanabe, H.; Suzuki, Y.; Saito, H. Magnetization of α-Phase Fe-Mn Alloys. *J. Phys. Soc. Jpn.* **1974**, *36*, 971−974.
(41) Paduani, C.; da Silva, E. G.; Perez-Alcazar, G. A. Mössbauer Effect Study of Gamma-FeMn Alloys. *Hyperfine Interact.* **1992**, *73*, 233−245.
(42) Ohno, H.; Mekata, M. Antiferromagnetism in Hcp Iron-Manganese Alloys. *J. Phys. Soc. Jpn.* **1971**, *31* (1), 102−108.
(43) Matsui, M.; Sato, K.; Adachi, K. Magnetic Properties of Fcc Gamma-Phase in Ternary Co-Mn-Fe System. *J. Phys. Soc. Jpn.* **1973**, *35* (2), 419−425.
(44) Marinelli, P.; Baruj, A.; Guillermet, A. F.; Sade, M. Lattice Parameters of Metastable Structures in Quenched Fe-Mn Alloys. Part I: Experimental Techniques, Bcc and Fcc Phases. *Zeitschrift fur Met.* **2000**, *91* (11), 957−962.
(45) Endoh, Y.; Ishikawa, Y. Antiferromagnetism of Gamma-FeMn Alloys. *J. Phys. Soc. Jpn.* **1971**, *30* (6), 1614−1627.
(46) Li, C.-M.; Sommer, F.; Mittemeijer, E. J. Characteristics of the γ→α Transformation in Fe−Mn Alloys. *Mater. Sci. Eng., A* **2002**, *325* (1−2), 307−319.
(47) Adachi, K.; Sato, K.; Matsui, M.; Mitani, S. Magnetic Properties of Fcc Co-Mn-Fe System. *IEEE Trans. Magn.* **1972**, *8* (3), 693−695.
(48) Ishikawa, Y.; Endoh, Y. Antiferromagnetism of Gamma-FeMn Alloys. II. Neutron Diffraction and Mossbauer Effect Studies. *J. Phys. Soc. Jpn.* **1967**, *23* (2), 205−213.
(49) Zimmerman, J. E.; Arrott, a.; Sato, H.; Shinozaki, S. Antiferromagnetic Transition in γ-Phase Mn Alloys. *J. Appl. Phys.* **1964**, *35* (3), 942.
(50) Hinomura, T.; Nasu, S.; Tomota, Y. ^{57}Fe Mossbauer Study of Gamma-FeMn and Epsilon-FeMn Alloys. *Nippon Kinzoku Gakkaishi* **1998**, *62* (7), 635−641.
(51) Umebayashi, H.; Ishikawa, Y. Antiferromagnetism of Gamma-FeMn Alloys. *J. Phys. Soc. Jpn.* **1966**, *21* (7), 1281−1294.
(52) Parr, J. G. Epsilon-FeMn. *J. Iron Steel Inst.* **1952**, *171* (137).
(53) Disclaimer: Any mention of commercial products within this paper is for information only; it does not imply recommendation or endorsement by NIST.

DOI: 10.1021/acsanm.8b02319
ACS Appl. Nano Mater. 2019, 2, 1940−1950

(54) Kouvel, J. S.; Kasper, J. S. Long-Range Antiferromagnetism in Disordered FeNiMn Alloys. *J. Phys. Chem. Solids* **1963**, *24* (5), 529–536.
(55) Azuah, R. T.; Kneller, L. R.; Qiu, Y.; Tregenna-Piggott, P. L. W; Brown, C. M.; Copley, J. R. D.; Dimeo, R. M. DAVE: A Comprehensive Software Suite for the Reduction, Visualization, and Analysis of Low Energy Neutron Spectroscopic Data. *J. Res. Natl. Inst. Stand. Technol.* **2009**, *114* (6), 341.
(56) Novak, G. A.; Colville, A. A. A Practical Interactive Least-Squares Cell-Parameter Program Using an Electronic Spreadsheet and a Personal Computer. *Am. Mineral.* **1989**, *74*, 488–490.
(57) Williamson, G. K.; Hall, W. H. X-Ray Line Broadening from Filed Aluminum and Wolfram. *Acta Metall.* **1953**, *1*, 22–31.
(58) Larson, A. C.; Von Dreele, R. B. *General Structure Analysis System (GSAS)*; Los Alamos National Laboratory Report LAUR 86-748; 2000.
(59) *Igor Pro Manual*. Wavemetrics Inc.: Lake Oswego, OR; https://www.wavemetrics.com/products/igorpro/manual
(60) Krycka, K.; Borchers, J.; Ijiri, Y.; Booth, R.; Majetich, S. Polarization-Analyzed Small-Angle Neutron Scattering. II. Mathematical Angular Analysis. *J. Appl. Crystallogr.* **2012**, *45* (3), 554–565.
(61) Butler, P.; Doucet, M.; Jackson, A.; King, S.; et al. SasView. http://www.sasview.org/.
(62) Skumryev, V.; Stoyanov, S.; Zhang, Y.; Hadjipanayis, G.; Givord, D.; Nogues, J. Beating the Superparamagnetic Limit with Exchange Bias. *Nature* **2003**, *423*, 850–853.
(63) Makhlouf, S. A.; Al-Attar, H.; Kodama, R. H. Particle Size and Temperature Dependence of Exchange Bias in NiO Nanoparticles. *Solid State Commun.* **2008**, *145*, 1–4.
(64) Kiwi, M. Exchange Bias Theory. *J. Magn. Magn. Mater.* **2001**, *234* (3), 584–595.
(65) McGrath, B. V.; Camley, R. E.; Wee, L.; Kim, J.-V.; Stamps, R. L. Temperature Dependence of Exchange Biased Thin Films. *J. Appl. Phys.* **2000**, *87* (9), 6430–6432.
(66) Stiles, M. D.; McMichael, R. D. Temperature Dependence of Exchange Bias in Polycrystalline Ferromagnet-Antiferromagnet Bilayers. *Phys. Rev. B: Condens. Matter Mater. Phys.* **1999**, *60* (18), 12950.
(67) Ohba, S.; Saito, Y.; Noda, Y. A Measurement of Charge Asphericity in Iron Metal. *Acta Crystallogr., Sect. A: Cryst. Phys., Diffr., Theor. Gen. Crystallogr.* **1982**, *38* (5), 725–729.
(68) NIST IGOR/DANSE. Ellipsoid Functions. http://www.sasview.org/docs/user/models/ellipsoid.html (accessed Jan 19, 2018).
(69) Porter, D. A.; Easterling, K. E.; Sherif, M. Y. *Phase Transformations in Metals and Alloys*, 3rd ed.; Routledge, 2009.
(70) Smith, C. S. Grain Shapes and Other Metallurgical Applications of Topology. *Metallogr., Microstruct., Anal.* **2015**, *4* (6), 543–567.
(71) Bonder, M. J.; et al.Magnetic Nanoparticles. In *Advanced Magnetic Nanostructures*; Sellmyer, D. J., Skomski, R., Eds.; Springer: Berlin, 2006; p 184.
(72) Schmid, I.; Kappenberger, P.; Hellwig, O.; Carey, M. J.; Fullerton, E. E.; Hug, H. J. The Role of Uncompensated Spins in Exchange Biasing. *Europhys. Lett.* **2008**, *81* (1), 17001.
(73) Doi, S.; Awaji, N.; Nomura, K.; Hirono, T.; Nakamura, T.; Kimura, H. Magnetization Profile in the MnIr/CoFe Exchange Bias System. *Appl. Phys. Lett.* **2009**, *94* (23), 232504.
(74) Takahashi, H.; Kota, Y.; Tsunoda, M.; Nakamura, T.; Kodama, K.; Sakuma, A.; Takahashi, M. Uncompensated Antiferromagnetic Moments in Mn-Ir/FM (FM = Ni-Co, Co-Fe, Fe-Ni) Bilayers: Compositional Dependence and Its Origin. *J. Appl. Phys.* **2011**, *110* (12), 123920.
(75) Malozemoff, A. P. Random-Field Model of Exchange Anisotropy at Rough Ferromagnetic-Antiferromagnetic Interfaces. *Phys. Rev. B: Condens. Matter Mater. Phys.* **1987**, *35* (7), 3679.
(76) Mauri, D.; Kay, E.; Scholl, D.; Howard, J. K. Novel Method for Determining the Anisotropy Constant of MnFe in a NiFe/MnFe Sandwich. *J. Appl. Phys.* **1987**, *62* (7), 2929.
(77) Chen, Y.; Lottis, D. K.; Dahlberg, E. D.; Kuznia, J. N.; Wowchak, A. M.; Cohen, P. I. Exchange Effects in Molecular-Beam-Epitaxy Grown Iron Films. *J. Appl. Phys.* **1991**, *69* (8), 4523–4525.
(78) Tsang, C.; Heiman, N.; Lee, K. Exchange Induced Unidirectional Anisotropy at FeMn-$Ni_{80}Fe_{20}$ Interfaces. *J. Appl. Phys.* **1981**, *52* (3), 2471–2473.
(79) Mauri, D.; Siegmann, H. C.; Bagus, P. S.; Kay, E. Simple Model for Thin Ferromagnetic Films Exchange Coupled to an Antiferromagnetic Substrate. *J. Appl. Phys.* **1987**, *62* (7), 3047.
(80) Lund, M. S.; Macedo, W. A. A.; Liu, K.; Nogués, J.; Schuller, I. K.; Leighton, C. Effect of Anisotropy on the Critical Antiferromagnet Thickness in Exchange-Biased Bilayers. *Phys. Rev. B: Condens. Matter Mater. Phys.* **2002**, *66* (5), 054422.
(81) Takahashi, M.; Tsunoda, M. Magnetic Anisotropy of Antiferromagnet and Its Role on the Exchange Bias in Ferromagnetic/Antiferromagnetic Bilayers. *J. Phys. D: Appl. Phys.* **2002**, *35* (19), 2365–2376.

DOI: 10.1021/acsanm.8b02319
ACS Appl. Nano Mater. 2019, 2, 1940–1950